

## Divergence of turbulent fluxes in the surface layer: case of a coastal city

G. Pigeon · A. Lemonsu · C. S. B. Grimmond ·  
P. Durand · O. Thouron · V. Masson

Received: 1 June 2006 / Accepted: 18 January 2007  
© Springer Science+Business Media B.V. 2007

**Abstract** This study quantifies the processes that take place in the layer between the mean building height and the measurement level of an energy balance micrometeorological tower located in the dense old core of a coastal European city. The contributions of storage, vertical advection, horizontal advection and radiative divergence for heat are evaluated with the available measurements and with a three-dimensional, high-resolution meteorological simulation that had been evaluated against observations. The study focused on a summer period characterized by sea-breeze flows that affect the city. In this specific configuration, it appears that the horizontal advection is the dominant term. During the afternoon when the sea breeze is well established, correction of the sensible heat flux with horizontal heat advection increases the measured sensible heat flux up to  $100 \text{ W m}^{-2}$ . For latent heat flux, the horizontal moisture advection converted to equivalent latent heat flux suggests a decrease of  $50 \text{ W m}^{-2}$ . The simulation reproduces well the temporal evolution and magnitude of these terms.

**Keywords** ESCOMPTE-UBL · Flux divergence · Horizontal and vertical advection · Sea breeze · Urban energy balance

---

G. Pigeon (✉) · A. Lemonsu · O. Thouron · V. Masson  
Centre National de Recherches Météorologiques, Météo-France/CNRS-GAME, 42 av. Coriolis,  
31057 Toulouse Cedex, France  
e-mail: gregoire.pigeon@meteo.fr

C. S. B. Grimmond  
Department of Geography, King's College London, WC2R 2LS London, UK

P. Durand  
Laboratoire d'Aérodynamique, UMR5560, CNRS - Université Paul Sabatier, Toulouse III  
Toulouse, France

## 1 Introduction

The surface energy balance (SEB) framework developed by Oke (1988) for urban areas applies to a control volume from the ground to the top of the urban canopy layer (UCL, Oke 1976)

$$Q^* + Q_F = Q_H + Q_E + \Delta Q_S + \Delta Q_A \quad (1)$$

where  $Q^*$ ,  $Q_H$  and  $Q_E$  are respectively, the net all-wave radiation, the turbulent sensible heat and latent heat fluxes at the top of the control volume,  $Q_F$  and  $\Delta Q_S$  are the anthropogenic heat releases and the net storage of heat within the control volume, and  $\Delta Q_A$  is the sum of advection of heat and moisture (converted to equivalent latent heat) through the sides of the control volume. This SEB framework is applied in the Town Energy Balance (TEB) model (Masson 2000) at the mean building height on horizontal scales of a few hundreds metres to a few kilometres (Fig. 1). The study of the urban SEB is necessary to improve the understanding of the urban heat island development and the structure of the urban boundary layer.

To make SEB measurements representative of mesoscale atmospheric model horizontal scales (typically a few hundreds metres to a few kilometres), micrometeorologists must take into account the vertical structure of the atmosphere that develops

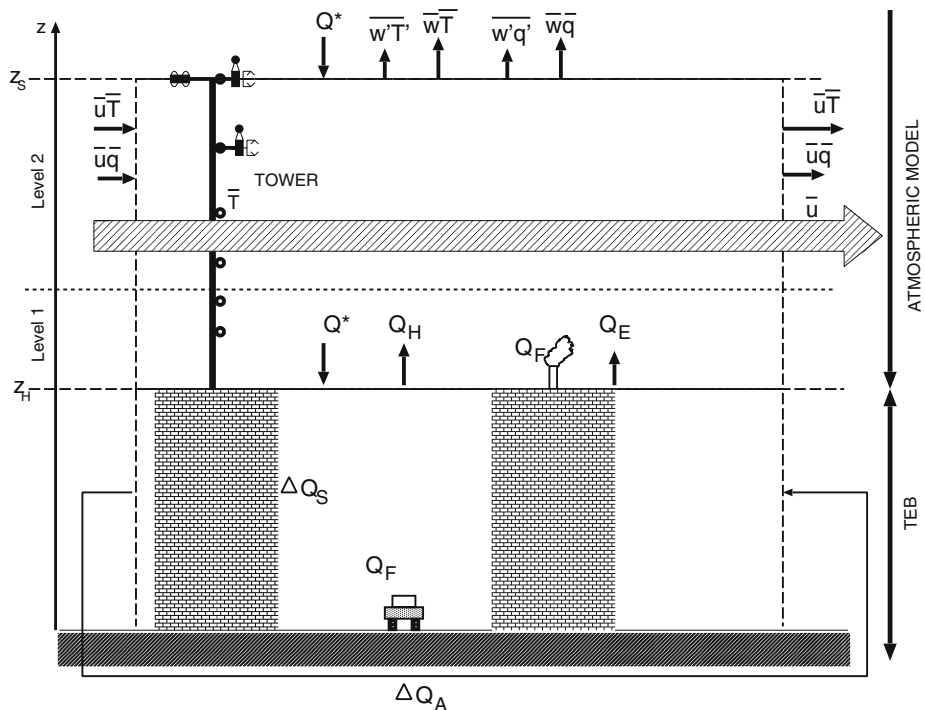


**Fig. 1** The urban surface energy balance proposed by Oke (1988) ( $Q^* + Q_F = Q_H + Q_E + \Delta Q_S + \Delta Q_A$ ) is applied in the TEB model (Masson 2000) at the mean building height  $z_H$  which is the base of the atmospheric model's first level. At the sensor level  $z_S$ , the turbulent and radiation fluxes may differ from  $z_H$  values because of horizontal and vertical advection, storage in the layer, or radiative divergence

above urban areas. Over tall canopies, a deep roughness sublayer (RSL) has been observed (Raupach et al. 1980; Roth 2000), and where meteorological parameters are influenced by the individual roughness elements. Above the RSL, which can be as high as four times the mean building height for certain canopy geometry (Oke 2004), an inertial sublayer (ISL) or a constant flux layer has been reported (Rotach 1993) as is the case over low roughness surfaces. Measurements conducted in this layer are representative of the local scale (a few hundreds metres), which is comparable to mesoscale model mesh size. With an increase of the measurement height, the risk of divergence between the measured turbulent and radiation fluxes and the corresponding terms of the SEB at the top of the UCL also increases. The layer between the top of the UCL and the measurement level can be affected by processes operating at different scales. First, this layer is the region where microscale processes blend together. Then, mesoscale processes such as sea-breeze circulations and drainage flows can also affect this layer, and can be evaluated by the application of the conservation equations of heat and moisture on a control volume that extends from the top of the UCL to the measurement height. Such a framework has been developed by Finnigan (2004). The processes that are taken into account in this approach are the storage of heat (or moisture) in the layer, and horizontal and vertical advection through the boundaries of the control volume (Fig. 1). These terms need to be quantified to correct the flux measurements and to retrieve the SEB at the top of the UCL. This volumic framework has been applied recently to field measurements (Lee 1998; Paw U et al. 2000; Aubinet et al. 2003; Feigenwinter et al. 2004) for the estimation of the net ecosystem exchange of carbon dioxide over forests. From these studies, vertical and horizontal advection appear to be terms that cannot be neglected in estimates of the net exchange of carbon dioxide especially at night. In these cases, advection often results from gravity flows at the local scale. Over urban areas, a recent attempt to quantify horizontal advection is presented by Spronken-Smith et al. (2006) for stable wintertime conditions.

Our study is based on the UBL-ESCOMPTE field campaign (Cros et al. 2004; Mestayer et al. 2005) that took place during June and July 2001 over the coastal agglomeration of Marseille in the south-east of France. During the field campaign a sea breeze was often observed and led to horizontal gradients of temperature and moisture aligned with the flow. The objective is to quantify the different processes that occur here in the layer between the top of the UCL and the measurement level of a tower located in the downtown area of Marseille under the influence of this mesoscale flow (Grimmond et al. 2004).

The theoretical framework, the method to compute each term, and the associated results are presented. The analysis is done using measurements, and a high-resolution numerical simulation [evaluated against observations (Lemonsu et al. 2006)] performed with the Meso-NH atmospheric model (Lafore et al. 1998) and coupled with the TEB model (Masson 2000; Lemonsu et al. 2004) for the representation of built-up areas.

## 2 Theory

The conservation of heat at a point can be written as (Stull 1988)

$$\frac{\partial \bar{\theta}}{\partial t} + \frac{\partial \overline{w'\theta'}}{\partial z} + \bar{u} \frac{\partial \bar{\theta}}{\partial x} + \bar{w} \frac{\partial \bar{\theta}}{\partial z} + \frac{1}{\bar{\rho} C_p} \frac{\partial Q^*}{\partial z} = 0 \quad (2)$$

where the  $x$ -axis has the orientation of the mean horizontal wind  $\bar{u}$  and the  $z$ -axis is oriented along the local vertical.  $\theta$  is the potential temperature,  $w$  is the vertical wind velocity component, the overbar is the Reynolds ensemble average operator and the prime denotes the turbulent deviation from this average.  $\bar{\rho}$  is the mean-air density,  $C_p$  is the specific heat at constant pressure of air and  $Q^*$  is the net all-wave radiation. The first term in Eq. 2 is the time derivative of the potential temperature and the second term is the vertical divergence of the vertical turbulent kinematic heat flux. The third and fourth terms are horizontal and vertical advection of heat, respectively and the last term is the vertical divergence of net radiation. The heat budget of the layer between the top of the UCL ( $z_H$ , hereafter) and the sensor level ( $z_S$ , hereafter) can be expressed in a general framework with a volumic integration of Eq. 2 over the footprint area of the measured turbulent fluxes in the horizontal, and from  $z_H$  to  $z_S$  in the vertical. For a single tower, an approximate heat budget of this layer can be derived by a one-dimensional integration of Eq. 2 from the surface to the measurement level (Lee 1998; Baldocchi et al. 2000; Finnigan 2004). This approximation will be made here since the characteristics of the surface cover in the footprint area are rather homogeneous (Lemonsu et al. 2004). The budget between  $z_H$  and  $z_S$  then is

$$\int_{z_H}^{z_S} \frac{\partial \bar{\theta}}{\partial t} dz + \int_{z_H}^{z_S} \frac{\partial \overline{w'\theta'}}{\partial z} dz + \int_{z_H}^{z_S} \bar{u} \frac{\partial \bar{\theta}}{\partial x} dz + \int_{z_H}^{z_S} \bar{w} \frac{\partial \bar{\theta}}{\partial z} dz + \int_{z_H}^{z_S} \frac{1}{\bar{\rho} C_p} \frac{\partial Q^*}{\partial z} dz = 0. \quad (3)$$

From the definition of the sensible heat flux at any height,  $Q_H(z) = \bar{\rho} C_p \overline{w'T'}(z)$  (Webb et al. 1980, hereafter WPL; Businger 1982) where  $T$  is the air temperature, and from Eq. 3, the  $Q_H$  term in the urban SEB at  $z_H$  (Eq. 1) can be expressed as a function of the sensible heat flux measured at  $z_S$  and four complementary terms

$$Q_H(z_H) = Q_H(z_S) + \frac{\bar{T}}{\bar{\theta}} \left[ \underbrace{\bar{\rho} C_p \int_{z_H}^{z_S} \frac{\partial \bar{\theta}}{\partial t} dz}_{\text{I}} + \underbrace{\bar{\rho} C_p \int_{z_H}^{z_S} \bar{u} \frac{\partial \bar{\theta}}{\partial x} dz}_{\text{II}} + \underbrace{\bar{\rho} C_p \int_{z_H}^{z_S} \bar{w} \frac{\partial \bar{\theta}}{\partial z} dz}_{\text{III}} + \underbrace{Q^*(z_S) - Q^*(z_H)}_{\text{IV}} \right], \quad (4)$$

where term I represents heat storage in the air layer, terms II and III are horizontal and vertical heat advection, and term IV results from the radiative divergence.

The same can be applied to the conservation of moisture

$$\frac{\partial \bar{q}}{\partial t} + \frac{\partial \overline{w'q'}}{\partial z} + \bar{u} \frac{\partial \bar{q}}{\partial x} + \bar{w} \frac{\partial \bar{q}}{\partial z} = 0 \quad (5)$$

where  $q$  is the specific humidity. The expression for the latent heat flux is  $Q_E(z) \approx \bar{\rho}_a L \overline{w'r'}(z)$  (WPL), where  $\bar{\rho}_a$  is the mean air density of dry air,  $L$  is the latent heat of vaporization and  $r$  is the mixing ratio of water vapour. In dry conditions, as over some cities, latent heat flux can be approximated as  $Q_E(z) \approx \bar{\rho} L \overline{w'q'}(z)$  and by integration

of Eq. 5, a similar relation is found between the turbulent latent heat flux measured at  $z_S$  and its value at  $z_H$

$$Q_E(z_H) = Q_E(z_S) + \bar{\rho}L \int_{z_H}^{z_S} \frac{\partial \bar{q}}{\partial t} dz + \bar{\rho}L \int_{z_H}^{z_S} \bar{u} \frac{\partial \bar{q}}{\partial x} dz + \bar{\rho}L \int_{z_H}^{z_S} \bar{w} \frac{\partial \bar{q}}{\partial z} dz. \quad (6)$$

In the case of  $Q_H$ , we quantify all the terms leading to divergence between  $z_H$  and  $z_S$  whereas for  $Q_E$ , with the available measurements, we are only able to estimate the storage of moisture in the air layer and horizontal advection. However, considering the small values measured for  $Q_E$  (see later results), we can assume that the vertical gradient of moisture is also small in the surface layer and that vertical advection should not be a dominant term in Eq. 6.

### 3 Method and results

#### 3.1 Field measurements and period of study

The UBL-ESCOMPTE field campaign is described in [Mestayer et al. \(2005\)](#) (see in particular their Fig. 1), and in this study, we concentrate on the CAA site located in the dense old city core of Marseille (Fig. 2) where a 25-m telescopic tower was mounted on a building and equipped with micrometeorological instrumentation ([Grimmond et al. 2004](#)). The top of the UCL ( $z_H$ ) of the 500 m area around the CAA site is 15.6 m. The equipment to measure the turbulent sensible and latent heat fluxes was installed at two levels (at the top of the tower and an intermediate level, which were at 43.9 and 37.9 m above the bottom of the street, respectively). A four-component radiometer (CNR1 from Kipp and Zonen) was set up at the top of the tower. The highest level is situated in the ISL ([Grimmond et al. 2004](#)) and is used in this study as the reference measurement level ( $z_S = 43.9$  m). Along the tower, the temperature profile was measured with thermocouples at six levels located between  $z_H$  and  $z_S$  (at 24.4, 26.9, 30.0, 34.2, 37.9 and 43.9 m above the street level). More details concerning the site can be found in [Grimmond et al. \(2004\)](#) and [Lemonsu et al. \(2004\)](#). A network of temperature and humidity sensors ([Pigeon et al. 2006](#)) located inside the streets at 6 m above the ground is used in the study (see site marked as T or q on Fig. 2). Two other stations (referenced as GLM and OBS sites, Fig. 2) equipped with micrometeorological instrumentation mounted on towers are also used to estimate the divergence of the horizontal wind.

Our analysis is applied to measurements from two intensive observation periods (IOP2a and IOP2b) of the ESCOMPTE field campaign. From 21 to 23 June 2001 (IOP2a), the synoptic situation is marked by the termination of a Mistral wind (from north-west) period, whereas from 24 to 26 June (IOP2b), the synoptic wind is variable and very weak. Both periods are marked by sunny weather and air temperatures up to 30 °C. A west to south-west sea breeze develops every afternoon. This phenomenon is of major interest for this study since it leads to horizontal gradients of temperature and moisture aligned with the wind direction. More details about the meteorological conditions are reported in [Lemonsu et al. \(2006\)](#). The turbulent sensible and latent heat fluxes measured during these IOPs are given in Figs. 11 and 12. Peak values of

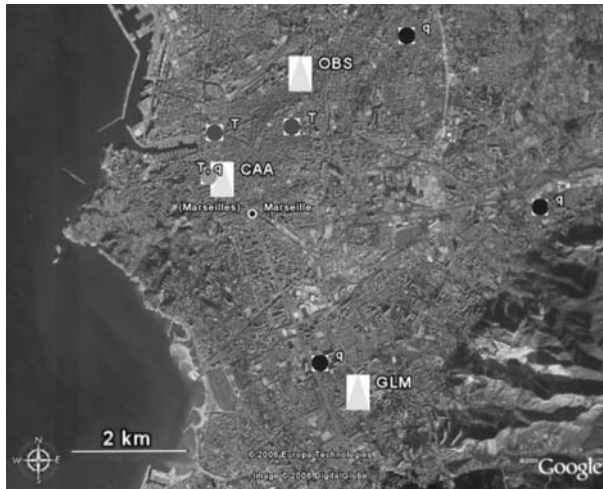


**Fig. 2** The city is bordered to the west by the Mediterranean sea. The focus of the study is on the CAA site (grey triangle) where an instrumented tower is located. Two towers labelled OBS and GLM (grey triangles) are used to estimate the horizontal gradient of wind speed. Then two sets of canopy stations allow the quantification of the horizontal gradient of moisture (black circles with q label) and temperature (dark grey circles with T label). One station is used for both gradients (grey circle with T, q label)

measured  $Q_H$  varied between 300 and 450  $\text{W m}^{-2}$  and night values are in general weakly positive. The measured  $Q_E$  is never greater than 200  $\text{W m}^{-2}$ .

### 3.2 Estimation of radiative divergence

#### 3.2.1 Radiation model

The shortwave radiation divergence in the layer from  $z_H$  to  $z_S$  is negligible: from the results of Roger et al. (2006) obtained during the same field campaign, even in the case of heavy polluted air when the divergence is the highest, the heating rate due to shortwave radiation divergence only reach 2.1  $\text{K day}^{-1}$  at the surface. This corresponds to a difference of 1  $\text{W m}^{-2}$  in net shortwave radiation between the top and the bottom of the layer. On the other hand, the longwave radiation divergence can lead to a significant cooling (heating) rate in the same layer consistent with a surface temperature anomaly (Frangi et al. 1992; Ha and Mahrt 2003; Savijärvi 2006). To quantify this phenomenon, we use the rapid radiative transfer model (RRTM, Mlawer et al. 1997). Simulations are performed with an eight-layer vertical profile. The definition of surface and near-surface temperatures (at the bottom of the first layer) are discussed in the following section (3.2.2). Then temperatures of the first six layers (between  $z_H$  and  $z_S$ ) are initialized with the measurements from the tower. The potential temperature is assumed to be constant in the layer between  $z_S$  and 100 m, and the downward longwave radiation at the top is prescribed in order to obtain the measured downward longwave radiation at  $z_S$ . Water vapour and carbon dioxide concentrations are assumed to be constant in the vertical, and their values are those measured at the top of the tower. The concentration and optical properties of aerosols are given by Mallet et al. (2003).

### 3.2.2 Surface and near-surface temperature estimates

To run RRTM, we have to estimate the urban surface temperature ( $T_{us}$ ). For an urban area, the surface is composed of a mix of roofs, walls and roads that have a large variability of orientations and properties. As a consequence, the computation of a representative  $T_{us}$  is complex (Voogt and Grimmond 2000).  $T_{us}$  can be estimated with the following equation

$$T_{us} = \left( \frac{L\uparrow - (1 - \varepsilon)L\downarrow}{\sigma \varepsilon} \right)^{\frac{1}{4}} \quad (7)$$

where  $\varepsilon$  is the average emissivity of the surface,  $\sigma$  is the Stefan–Boltzmann constant ( $5.67 \times 10^{-8} \text{ W m}^{-2} \text{ K}^{-4}$ ) and  $L\downarrow$  ( $L\uparrow$ ) is the surface downward (upward) longwave flux. Emissivities in a 500-m radius circle around the tower site were 0.94 for roads, 0.90 for roofs, 0.90 for walls (Lemonsu et al. 2004). Considering the fraction of each surface in this area, a global emissivity of 0.91 is estimated. From Grimmond et al. (2004), outgoing longwave radiation is the same regardless of sensor height. Since a sensor height change is equivalent to a footprint change, we conclude that emissivity is homogeneous in the area sampled by the measurement.

A first estimate of  $T_{us}$  is computed using (7), assuming that  $L\downarrow$  and  $L\uparrow$  at the surface were equal to those at  $z_S$ . Due to the absorption in the layer, this assumption is not correct, so we have adjusted  $T_{us}$  by an iterative process in order to reproduce, with the simulation,  $L\uparrow$  observed at  $z_S$ . It is possible to use this criterion to adjust  $T_{us}$  because the radiative divergence is not significantly sensitive to air composition change in the layer (see next section). Nevertheless, the nighttime surface temperature estimated by this method is lower than air temperature (Fig. 4), which is not consistent with the generally upward turbulent heat flux measured during the night (see later results). This inconsistency is probably due to the difference between the turbulent and radiative footprint areas and/or the accuracy of the sensor ( $\pm 5\%$  according to Kohsiek et al. 2007). Consequently, the surface temperature has been adjusted by an offset (+6.5 K) so that nighttime values are consistent with the observed turbulent heat flux.

The near-surface temperature also needs to be initialized in the simulation (Ha and Mahrt 2003; Savijärvi 2006). Besides the levels indicated in Sect. 3.1, there was an air temperature measurement at  $z_H$  (at the top of the canyon) during the field campaign but it failed during IOP2a and IOP2b. Hence, we have to estimate the air temperature at  $z_H$ . The best estimate is a linear model for which input data are: (1) the lowest available level of air temperature measured along the tower during IOP2a and IOP2b (24.4 m above the street), and (2) the temperature measured in a canyon (at 6 m above the street) 100 m from the site (Fig. 2). The coefficients are computed with a multiple linear regression for the periods when the temperature measured at  $z_H$  is available. The model gives very consistent results with a correlation coefficient with observations of 0.98 (Fig. 3).

### 3.2.3 Results

In the case of a warm surface anomaly (higher than 3 K), a positive radiative divergence between  $z_S$  and  $z_H$  (Fig. 4) is computed in agreement with Frangi et al. (1992) and Savijärvi (2006). The highest values are  $30 \text{ W m}^{-2}$ , what is high enough to have

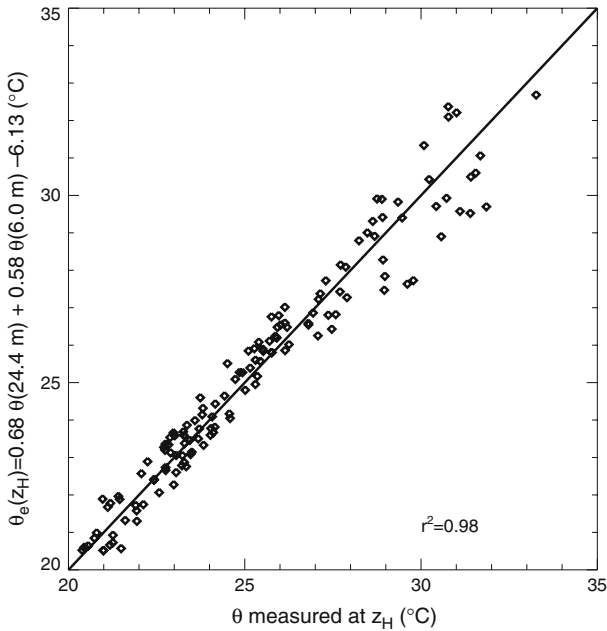


**Fig. 3** Comparison of air potential temperature measured at  $z_H$  and an estimate of this temperature ( $\theta_e(z_H)$ ) computed as a linear combination of air canyon potential temperature ( $\theta(6\text{ m})$ ) and above canyon air potential temperature ( $\theta(24.4\text{ m})$ ). The solid line represents the 1:1 relation. The correlation between measured value and its estimate is 0.98

to be taken into consideration in the energy budget of the surface layer. For the other conditions, the radiative divergence leads to radiative cooling in the layer. As mentioned in the preceding section, the estimation of the surface temperature is complex and results obtained with the first estimate of surface temperature are presented as a sensitivity test to this parameter. A variation of 6.5 K leads to an average difference of radiative divergence of  $12\text{ W m}^{-2}$ . A sensitivity test to the global emissivity was also conducted. A change of surface emissivity to the value of 1 has an impact of  $-2\text{ W m}^{-2}$ . The sensitivity to the composition of the air was also studied (Fig. 4). A strong increase of the optical thickness of aerosol particles, a doubled concentration of carbon dioxide or a variation of concentration of water vapour have no significant effect (lower than  $2\text{ W m}^{-2}$ ) on the radiative divergence.

### 3.3 Estimation of heat and moisture storage in the air

#### 3.3.1 Method

The heat storage in the air (term I of Eq. 4) is computed using the measured and estimated temperature profile (see 3.2.2). Then, the heat storage term is computed assuming a linear variation of temperature between each level. The storage of moisture is estimated with measurement of specific humidity at  $z_S$  assuming  $\frac{\partial q}{\partial t}$  is constant with height.

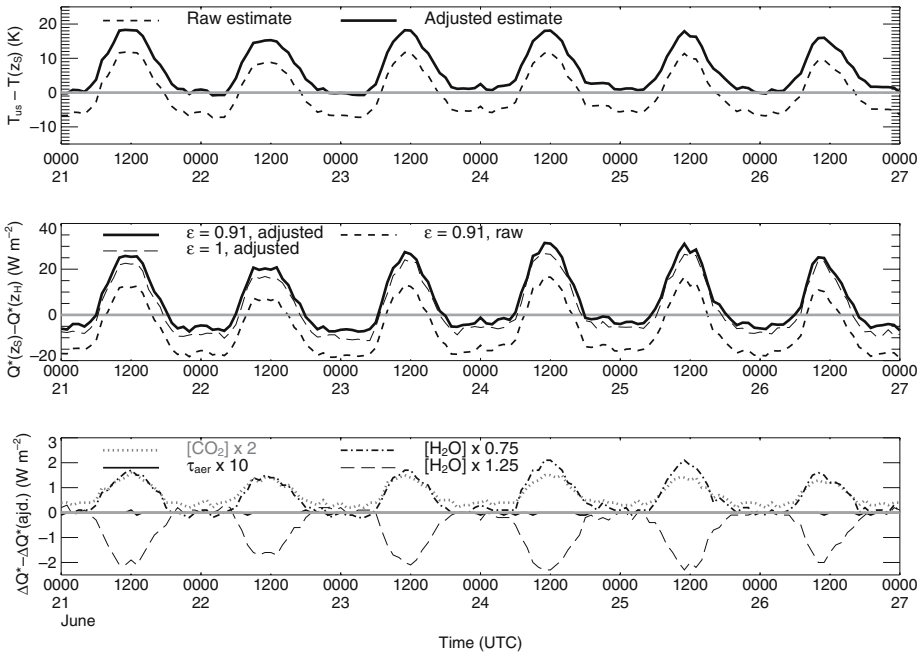


**Fig. 4** Variation of temperature difference between the urban surface and the air (top) and radiative divergence (middle, term IV of Eq. 4) during IOP2a and IOP2b (hourly basis). The “raw” estimate is computed with the surface temperature retrieved by inversion of the radiation measurements (see details in the text). The adjusted estimate is computed with the surface temperature in agreement with the nighttime sensible heat flux. In the middle frame, the long-dashed line represents the divergence computed with the emissivity set to 1. The bottom frame gives the impact on the radiative divergence of a doubling of carbon dioxide concentration, of an increase by a factor of 10 of the aerosol optical thickness, and of an increase (decrease) of water vapour concentration by a factor of 1.25 (0.75)

### 3.3.2 Results

The heat storage term (Fig. 5) is small ( $\pm 10 \text{ W m}^{-2}$ ) in comparison to the measured fluxes (see later results). This term has a positive contribution during the morning when the air between  $z_H$  and  $z_S$  becomes warmer and a smaller negative contribution during the cooling period.

The moisture storage converted to its equivalent latent heat (Fig. 6) is more variable but has a positive contribution each afternoon during the sea-breeze period. The values of this term are also small ( $\pm 15 \text{ W m}^{-2}$ ) in comparison to the measured fluxes (see later results).

## 3.4 Estimation of the vertical heat advection

### 3.4.1 Vertical velocity

The estimation of the vertical advection term (term III of Eq. 4) has recently received much attention (Lee 1998; Finnigan 1999; Paw U et al. 2000; Lee et al. 2004). In this term, the most problematic task is to evaluate a representative vertical velocity profile. In this section, we propose a framework to estimate the vertical velocity and

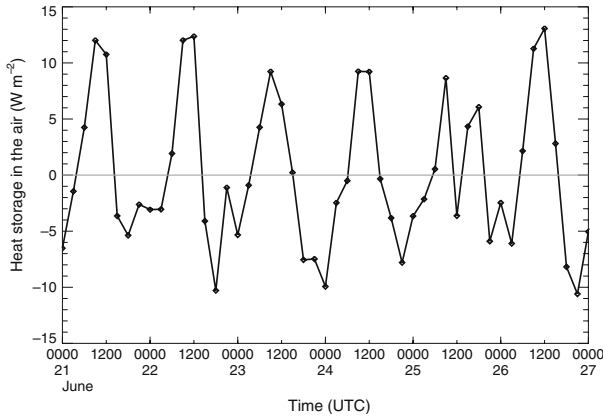


**Fig. 5** Heat storage in the air during IOP2a and IOP2b computed with the tower air temperature profile and an estimate of the air temperature at  $z_H$  (three-hourly averages reported)

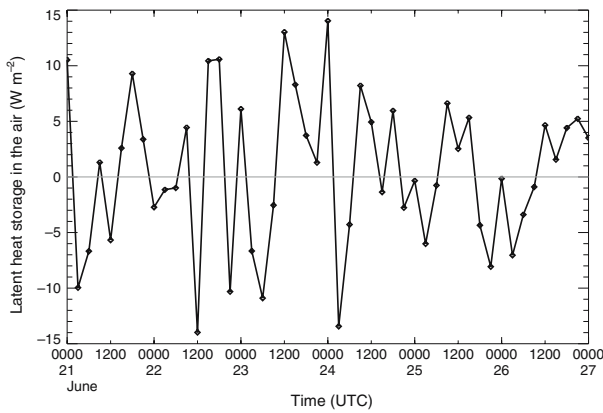


**Fig. 6** Moisture storage in the air converted to latent heat equivalent and computed with specific humidity measured at  $z_S$  (three-hourly averages reported)

the vertical advection adapted to the conditions of this study. First, we assume dry air because of the characteristics of this urban environment. Then, starting with a hypothesis of stationarity and using the Reynolds decomposition, the equation of mass conservation (the  $x$ -axis is aligned with the horizontal wind) is

$$\frac{\partial \bar{\rho} \bar{u}}{\partial x} + \frac{\partial \bar{\rho}' u'}{\partial x} + \frac{\partial \bar{\rho} \bar{w}}{\partial z} + \frac{\partial \bar{\rho}' w'}{\partial z} = 0. \tag{8}$$

According to Paw U et al. (2000), we assume that  $\frac{\partial \bar{\rho} \bar{u}}{\partial x} \gg \frac{\partial \bar{\rho}' u'}{\partial x}$ , and integration of Eq. 8 from  $z_H$  to  $z$  leads to

$$\bar{\rho}(z) \bar{w}(z) \approx -\overline{\rho' w'}(z) - \int_{z_H}^z \frac{\partial \bar{\rho} \bar{u}}{\partial x} dh \tag{9}$$

assuming that the  $z_H$  level is the reference surface and that there is no flux of dry air through this surface (WPL). From observations made during the field campaign, we

have  $\bar{\rho} \frac{\partial \bar{u}}{\partial x} \approx -10^{-4} \text{ kg m}^{-3} \text{ s}^{-1}$  and  $\bar{u} \frac{\partial \bar{\rho}}{\partial x} \approx -\frac{\bar{u} \bar{\rho}}{\bar{T}} \frac{\partial \bar{T}}{\partial x} \approx 10^{-7} \text{ kg m}^{-3} \text{ s}^{-1}$ . Moreover, neglecting the variation of density with height in the last term of Eq. 9 and considering that fluctuations of density are mainly driven by fluctuations in temperature, the vertical velocity can be approximated as

$$\bar{w}(z) \approx \frac{\overline{w'T'}}{\bar{T}} - \int_{z_H}^z \frac{\partial \bar{u}}{\partial x} dh. \tag{10}$$

In Eq. 10, the first term on the right-hand side has the same expression as in WPL in the case of a dry environment. The second term results from the horizontal divergence of the wind speed and is the only term considered in an incompressible framework. We present the estimation of these two terms separately.

### 3.4.2 Vertical advection resulting from WPL velocity

The WPL velocity (Eq. 10) is evaluated with measurements of the turbulent vertical kinematic heat flux and the air temperature at  $z_S$ . To first order, we assume that this term is constant from  $z_H$  to  $z_S$  and the resulting vertical advection term (term III of Eq. 4) is

$$\frac{\bar{T}}{\bar{\theta}} \bar{\rho} C_p \int_{z_H}^{z_S} \frac{\overline{w'T'}}{\bar{T}} \frac{\partial \bar{\theta}}{\partial z} dz \approx \frac{\bar{T}}{\bar{\theta}} \bar{\rho} C_p \left( \frac{\overline{w'T'}}{\bar{T}} \right)_{z_S} (\bar{\theta}(z_S) - \bar{\theta}(z_H)), \tag{11}$$

where  $\left( \frac{\overline{w'T'}}{\bar{T}} \right)_{z_S}$  is the measurement at  $z_S$ .

### 3.4.3 Vertical advection resulting from horizontal divergence of wind speed

The divergence of horizontal wind results, (i) from urban canopy changes in density or height (Coceal and Belcher 2004), (ii) from the increase of stress at the sea–land transition, and (iii) from the variation of the boundary-layer height from sea to land. The first cause acts at the local scale. Coceal and Belcher (2004) have demonstrated that it is small beyond a distance  $3L_c$  where  $L_c = \frac{z_H(1-\lambda_p)}{\lambda_f}$  ( $\lambda_p$  being the building plan area density and  $\lambda_f$  the total frontal area per unit ground area). From Lemonsu et al. (2004), we can estimate that  $L_c$  in the 500 m radius circle around the site varies between 15.7 and 22.2 m. The structure around the site can be seen from images in Grimmond et al. (2004) (their Fig. 1) and no significant change of density nor height of the urban canopy is noted at a distance below  $3L_c$ . Consequently, we assume that there is no divergence of the horizontal wind due to urban canopy changes. However, at a larger scale, the sea–land transition and orography can induce wind field variations. The divergence of horizontal wind at any height  $z$  between  $z_H$  and  $z_S$  can be estimated from the measurements as

$$\left( \frac{\partial \bar{u}}{\partial x} \right) (z) \approx \left( \frac{\partial \bar{u}}{\partial x} \right)_{z_S} \left( \frac{\ln \frac{z-d}{z_0}}{\ln \frac{z_S-d}{z_0}} \right), \tag{12}$$

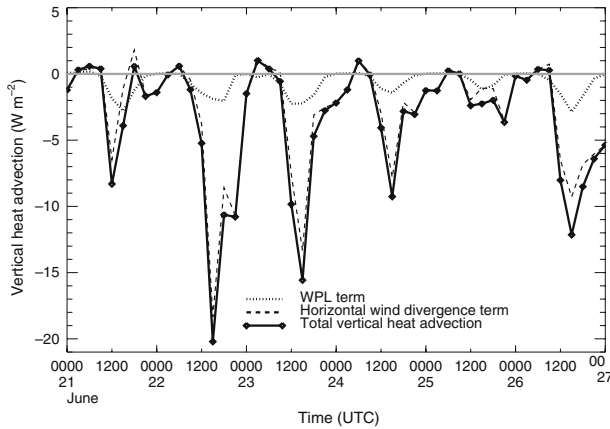


**Fig. 7** Estimation of the vertical heat advection (three-hourly average): term resulting from the WPL velocity, term resulting from the horizontal wind divergence and the total vertical advection computed as the sum of the two terms

where  $\left(\frac{\partial \bar{u}}{\partial x}\right)_{z_S}$  is the horizontal divergence of horizontal wind computed using measurements made at CAA, OBS and GLM (Fig. 2) that are at a comparable  $\frac{z_S}{z_H}$  level of 2.8 (Mestayer et al. 2005),  $d$  is the zero-plane displacement estimated from  $d = 0.7z_H$  ( $d = 10.9$  m, Grimmond et al. 2004) and  $z_0$  is the aerodynamic roughness length estimated by Grimmond et al. (2004) ( $z_0 = 2.5$  m). The resulting vertical advection term is

$$\begin{aligned} & \frac{\bar{T}}{\bar{\theta}} \bar{\rho} C_p \int_{z_H}^{z_S} - \left( \int_{z_H}^z \frac{\partial \bar{u}}{\partial x} dh \right) \frac{\partial \bar{\theta}}{\partial z} dz \\ & \approx - \frac{\bar{T}}{\bar{\theta}} \bar{\rho} C_p \left( \frac{\partial \bar{u}}{\partial x} \right)_{z_S} \frac{1}{\ln \frac{z_S - d}{z_0}} \int_{z_H}^{z_S} \left( \int_{z_H}^z \ln \frac{h - d}{z_0} dh \right) \frac{\partial \bar{\theta}}{\partial z} dz, \end{aligned} \quad (13)$$

and is computed using the temperature profile measured along the tower.

### 3.4.4 Results

Estimates of vertical advection are given in Fig. 7, where both contributing terms have a negative contribution with a minimum around 1500 UTC. At night both estimates are close to zero. The WPL term is small (few  $W m^{-2}$ ) whereas the horizontal wind divergence term is larger, with midday values around  $-15 W m^{-2}$ . However, in comparison to the measured sensible heat flux (Fig. 11) it is still small. Moreover, midday values will be compensated in part by the radiative divergence that is of the same order of magnitude but with a positive contribution.

## 3.5 Estimation of horizontal heat and moisture advection

### 3.5.1 Method based on observation

To estimate horizontal heat and moisture advection (term II in Eq. 4 and the similar term in Eq. 6), measurements of the horizontal gradients of temperature and moisture

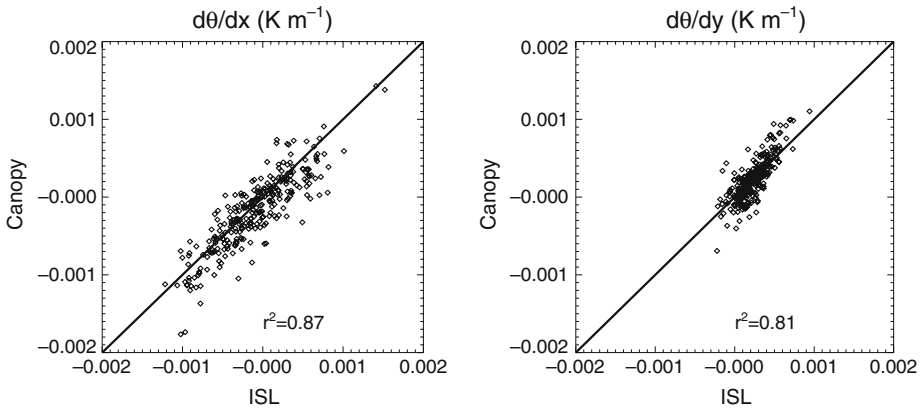


**Fig. 8** Comparison of the horizontal gradient of potential temperature measured in the canopy and in the ISL: zonal gradient (left) and meridional gradient (right). Solid line is the 1:1 relation

are required, as well as the wind profile. It is assumed that the horizontal gradients are driven by the sea-breeze circulation and that they are constant in the surface layer from the ground to  $z_S$ . This assumption is verified by comparing the horizontal gradient computed from the three tower sites OBS, GLM and CAA with that computed from the three closest stations of the canopy network. The results are presented in Fig. 8 for temperature. The good correlation between the estimate of the gradient at the two levels supports this assumption. Consequently, horizontal gradients are computed with subsets of the canopy station network. The three closest stations to the CAA site (Fig. 2) are used to compute horizontal gradient of temperature. In terms of moisture, it is not possible to estimate the gradient from the same subset of stations since measured differences between these stations are of the same order as the accuracy of the sensors (3% in relative humidity, see Table I of Pigeon et al. (2006) for results of the intercomparison of sensors). Another subset with more distant stations is used to quantify the horizontal gradient of moisture (Fig. 2).

The wind profile from  $z_H$  to  $z_S$  is computed using the measurement at 43.9 m above the bottom of the street and the relations that can be applied below that height. Grimmond et al. (2004) show that the momentum fluxes measured at 37.9 and 43.9 m are comparable, and conclude that these two levels are in the ISL. In another operational mode of the tower, the momentum fluxes were measured at 34.6 and 28.5 m, and in this case the momentum fluxes are dissimilar. We can then conclude that at least the lowest level of this mode is in the RSL and that the top of the RSL ( $z^*$ ) lies between 28.5 m and 37.9 m. Here for  $z^*$  we use the mean of these two values, i.e. 33.2 m above the street. The vertical wind profile is computed separately for the part of the layer that is in the RSL and for the part that is in the ISL. In the RSL, from  $z_H$  to  $z^*$ , we adopt a local scaling (Rotach 1993, 2001)

$$\frac{\partial \bar{u}}{\partial z} = \frac{u_{*,l}(z)}{kz} \tag{14}$$

where  $u_{*,l}(z)$  is the local friction velocity computed according to Rotach (2001)

$$\left( \frac{u_{*,l}(z)}{u_*^{IS}} \right)^3 = \sin \left( \left( \frac{\pi}{2} \right) \frac{z-d}{z^*-d} \right)^{1.28} \tag{15}$$

where  $u_*^{IS}$  is the friction velocity in the ISL and  $d$  is the zero-plane displacement. In the ISL, between  $z^*$  and  $z_S$ , we use the classic log-law profile. The stability effect on the wind profile is neglected here since it has a very low impact on the estimate of advection. The computation to evaluate the horizontal advection can therefore be expressed as

$$\begin{aligned} \frac{\bar{T}}{\bar{\theta}} \bar{\rho} C_p \int_{z_H}^{z_S} \bar{u} \frac{\partial \bar{\theta}}{\partial x} dz = \frac{\bar{T}}{\bar{\theta}} \bar{\rho} C_p \left( \frac{\partial \bar{\theta}}{\partial x} \right)_c \left[ \int_{z_H}^{z^*} \left( \bar{u}(z^*) - \int_z^{z^*} \frac{u_{*,l}(h)}{kh} dh \right) dz \right. \\ \left. + \int_{z^*}^{z_S} \left( \frac{u_*^{IS}}{k} \ln \frac{z-d}{z_0} \right) dz \right] \end{aligned} \quad (16)$$

where  $\left( \frac{\partial \bar{\theta}}{\partial x} \right)_c$  is the horizontal gradient measured at the canopy level. A similar formulation is adopted for the computation of the horizontal advection of moisture.

### 3.5.2 Numerical simulation

Since horizontal heat and moisture advection are the dominant terms in this study (see next section) they are evaluated independently in a numerical simulation for IOP2a and IOP2b of the field campaign. The simulation (Lemonsu et al. 2006) is performed with the atmospheric model Meso-NH (Lafore et al. 1998) in a grid-nesting mode to a horizontal resolution of 250 m over Marseille. The atmospheric model is coupled with TEB (Masson 2000; Masson et al. 2002; Lemonsu et al. 2004) for the representation of built-up areas and ISBA (Noilhan and Mahfouf 1996) for the representation of other surfaces. The exact settings and the evaluation of the simulation against the available measurements are presented in Lemonsu et al. (2006). The bottom of the atmospheric model, where the energy budget computed by TEB is assigned, is at the roof level  $z_H$  (Fig. 1). The second level of the atmospheric model is 25 m (i.e. 40.6 m above the ground) and corresponds approximately to the measurement level  $z_S$  (43.9 m). Horizontal heat and moisture advection is then calculated on an hourly basis for the two first levels of the atmospheric model. The mesh point closest to the tower location is taken to estimate the horizontal advection at the measurement site.

### 3.5.3 Results for horizontal heat advection

Horizontal heat advection (Fig. 9) has a diurnal cycle with maximum values in early afternoon and a very small contribution during the night. The two independent estimates (observation and simulation) are well correlated. The maximum values reached are much more important than the other terms and reveal the preponderance of horizontal advection in this study: on four days it reaches or surpasses  $100 \text{ W m}^{-2}$  for observations and simulation.

### 3.5.4 Results for horizontal moisture advection

The influence of the sea breeze, which is significant for heat, also applies to moisture, since the flow advects both cool and moist air from the sea. Fig. 10 shows the estimated horizontal advection of moisture (converted to latent heat equivalent as in (6)) by

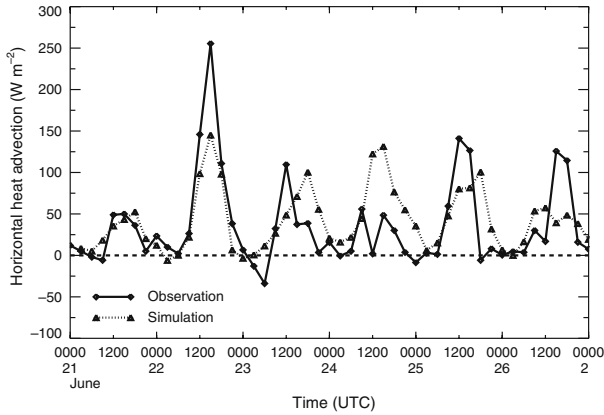


**Fig. 9** Horizontal heat advection (three-hourly average) computed with observations (solid line) and in the numerical simulation (dotted line)

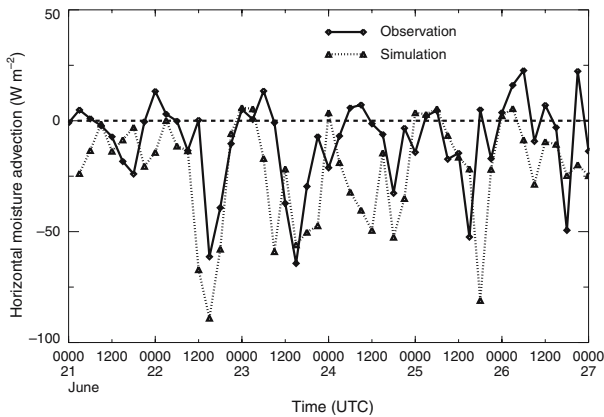


**Fig. 10** Horizontal moisture advection (three-hourly average) expressed in latent heat equivalent computed from the measurements of horizontal gradient of moisture and wind (solid line) and in the numerical simulation (dotted line)

both measurements and numerical simulation. Horizontal moisture advection has a negative contribution. Maximum amplitudes are also recorded in the early afternoon, whereas at night the signal is very weak. Comparison between observations and simulation are consistent even though the simulation has a tendency to produce a stronger influence of this term during afternoon. The minimum estimated values are between  $-50$  and  $-90 \text{ W m}^{-2}$ .

## 4 Physical analysis

### 4.1 Interpretation

The different terms evaluated with observations to adjust the fluxes from the measurement level to the mean building height have been taken into account to correct

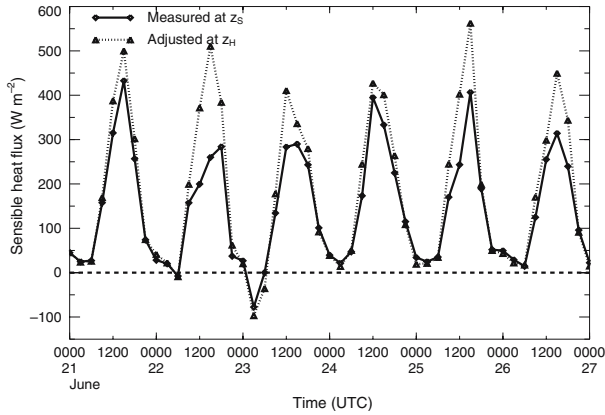


**Fig. 11**  $Q_H$  measured at  $z_S$  (solid line) and adjusted at  $z_H$  (dotted line) three hourly

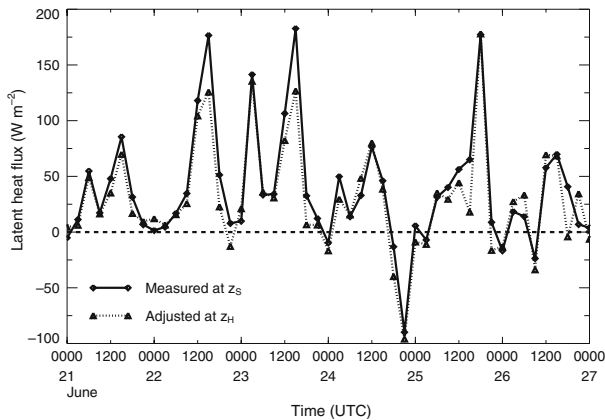


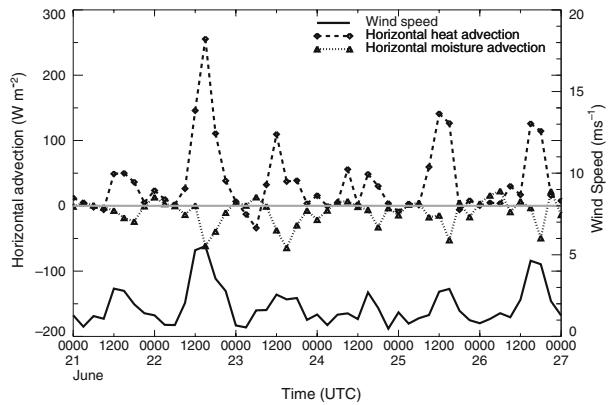
**Fig. 12**  $Q_E$  measured at  $z_S$  (solid line) and adjusted at  $z_H$  (dotted line) three hourly

sensible and latent heat fluxes. In Fig. 11, the measured and adjusted  $Q_H$  are compared. As described previously, the impact of the correction is larger during the day than during the night, especially for the second day of IOP2a. After correction, the adjusted flux reaches comparable maximum values on every day. This is consistent with the fact that the general forcing (radiation, synoptic weather) does not evolve significantly during the period. The measured and adjusted  $Q_E$  are shown in Fig. 12; the correction tends to reduce  $Q_E$  during the day. If we had applied the correction computed from the numerical simulation, the impact would have been higher. This seems quite consistent with the very dry environment of the study site for which vegetation occupied a plan area fraction of 0.136 (Lemonsu et al. 2004).

Corrections of  $Q_H$  ( $Q_E$ ) present a comparable day-to-day variability that is correlated (anti-correlated) with the sea-breeze intensity (Fig. 13). The largest horizontal advection of heat or latent heat is recorded for 22 June 2001 when the sea breeze reaches its maximum intensity.

Figure 14 presents a west-to-east vertical cross-section of simulated potential temperature and mixing ratio fields above the measurement site and a conceptual scheme

**Fig. 13** Comparison of the evolution of the horizontal heat and moisture (converted to the equivalent latent heat) advection and the wind speed during IOP2a and IOP2b



of the phenomenon that is occurring. The contribution of horizontal heat advection during the afternoon shows that a component of  $Q_H$  at  $z_H$  does not reach  $z_S$ . This component of  $Q_H$  warms the cool sea-breeze flow. The horizontal temperature gradient aligned with the wind results from the progressive heating of the flow as it progresses farther inland, and leads to an underestimation of the sensible heat flux with the instrumental configuration.

In contrast, the contribution of moisture horizontal advection leads to an overestimation of  $Q_E$  with the instrumental configuration. A component of  $Q_E$  measured at  $z_S$  does not derive from evaporation of water at the surface but results from the transport of moisture by the sea-breeze flow. The horizontal moisture gradient opposite to the wind results from the dilution of the water vapour contained in the sea-breeze flow in a deeper boundary layer as it progresses farther inland. Entrainment of dry air at the top of the boundary layer can also induce a positive vertical derivative of  $w'q'$  and lead to  $Q_E$  values measured at  $z_S$  higher than those at  $z_H$ .

#### 4.2 Spatial variation of horizontal advection

Since the existence of strong horizontal advection results from the sea-land transition and the sea breeze, it is interesting to estimate the relation between horizontal advection and the distance inshore. In Fig. 15 we show the horizontal heat advection, computed with measurements (symbols) and numerically (solid lines) as a function of the distance inshore. For each day, the horizontal advection is averaged over the period from 0900 to 1600 UTC. In the observations, the gradient is estimated using various stations in the temperature and moisture network (Pigeon et al. 2006) and the wind profile from the CAA site. For both the observations and the model, the distance from an inshore point to the sea has been computed along the wind direction. For the first few hundreds of metres from the sea, the horizontal heat advection is strong and can reach values higher than  $200 \text{ W m}^{-2}$ . After a distance of 2 km inshore, the horizontal advection of heat remains quite steady between  $40$  and  $100 \text{ W m}^{-2}$  for the model, and between  $20$  and  $80 \text{ W m}^{-2}$  for the observations. The model provides a better representation of the spatial variability: the field of horizontal heat advection for the 22 June at 1100 UTC is presented in Fig. 16. The highest values of horizontal advection (represented with darker grey) are located along the shoreline (solid line).

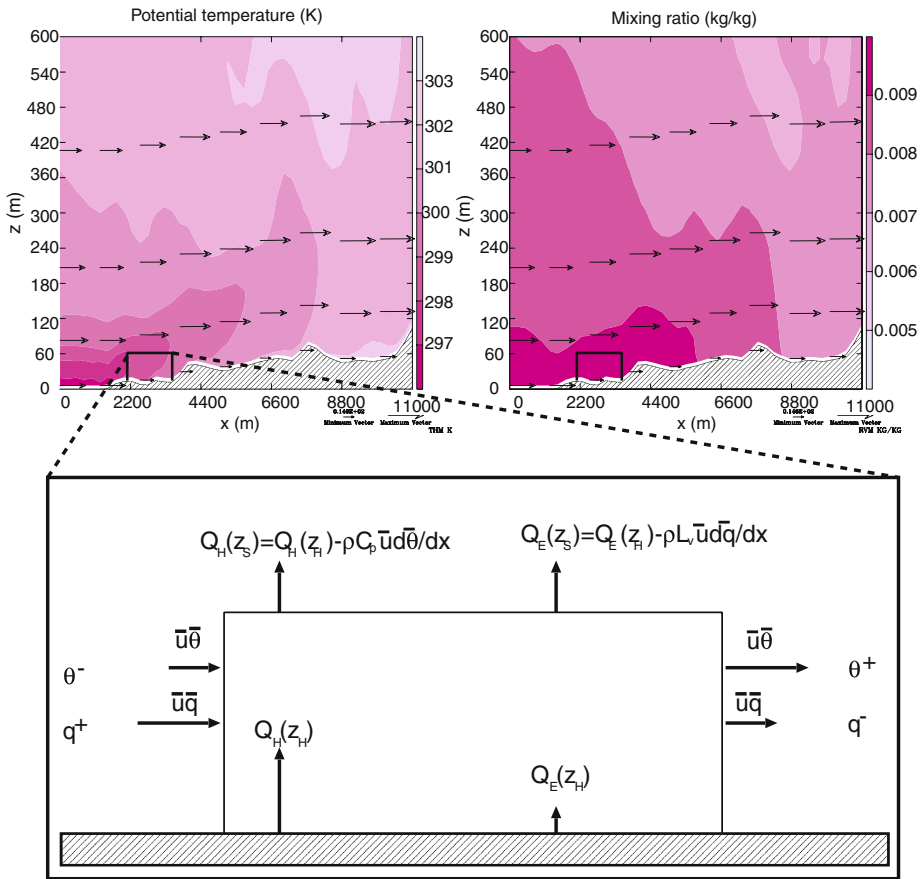


**Fig. 14** West-to-east vertical cross-section at the latitude of the CAA site in the simulation (top graphs). Mean potential temperature (top left) and mixing ratio (top right) between 1200 and 1500 UTC for the 22 June 2001. Arrows represent the westerly wind (longest arrow is equivalent to a  $4.8 \text{ m s}^{-1}$  wind speed and smallest  $1.4 \text{ m s}^{-1}$ ). The boxes indicates the control volume on which the budget of heat and moisture is calculated (bottom)

As presented in Fig. 15, after about 2 km inshore, the variation of horizontal advection becomes smoother.

### 5 Comparison with other studies

The integration of the conservation equations on a control volume and the estimation of the different terms of storage, vertical and horizontal advections have mainly been applied to species such as  $\text{CO}_2$ . Lee (1998) assumed horizontal homogeneity and focused on the influence of vertical advection when he considered the correlation between the corrected measured vertical velocity and the imbalance of the surface energy budget. Subsequently, Lee and Hu (2002) applied the same approach to estimate the vertical heat and moisture advection, and found a weak but statistically

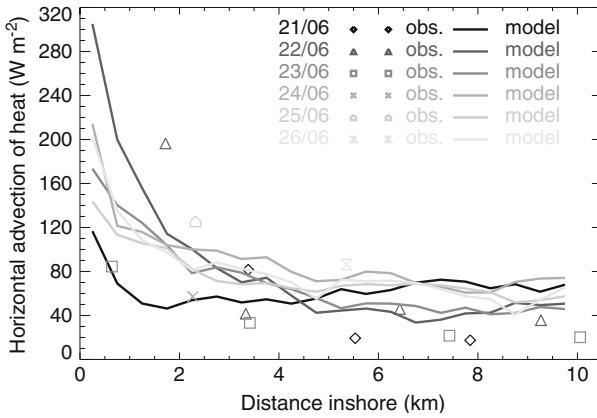


**Fig. 15** Variation of horizontal advection of heat with distance inshore computed from measurements and from the model for individual days from 0900 to 1600 UTC

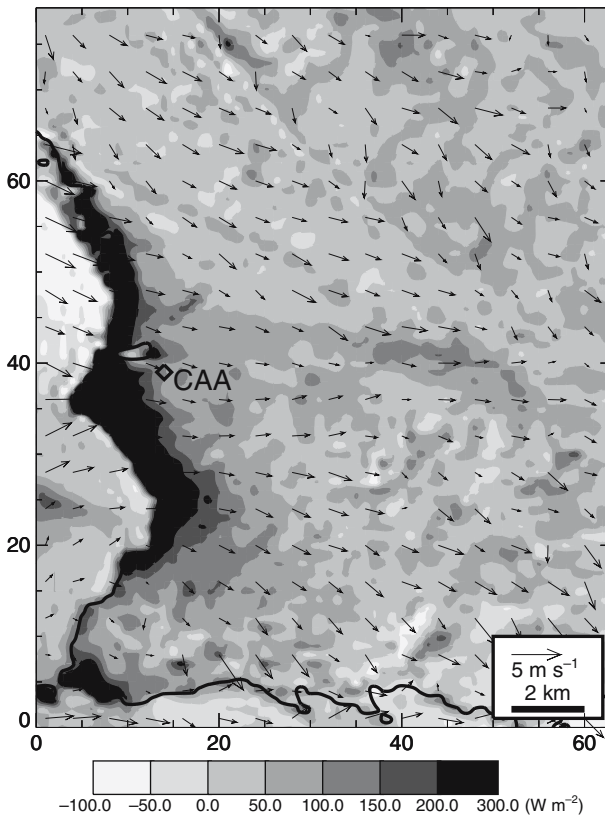


**Fig. 16** Simulated field of horizontal heat advection for the 22 June 2001 at 1100 UTC (hourly average). Values of horizontal advection of heat are represented as grey levels and wind direction and intensity with arrows

significant correlation between the energy budget imbalance and the vertical advection. The same approach has been applied by Rotach et al. (2003) for complex topography and, in their study, the impact of vertical advection on imbalance was of major concern. They computed vertical heat advection of the same order as this study but their estimation was associated with a positive vertical advection.

Paw U et al. (2000) developed a theoretical framework based on Lee (1998) and WPL. They studied vertical heat advection (their Fig. 6) and found results very comparable to the present study, with a negative peak around midday ( $-80 \text{ W m}^{-2}$ ) slightly greater than our values. Nevertheless, in their study the influence of horizontal advection is not taken into account since they supposed scalar homogeneity. For  $\text{CO}_2$  fluxes, the Aubinet et al. (2003, 2005) studies of both vertical and horizontal advection mainly attributed results to topography. They concluded that the two terms were opposite but of the same order.

The study of Spronken-Smith et al. (2006) is more comparable to this investigation but the approach is quite different. They started from the urban energy balance on a control volume developed by Oke (1988) and made an estimate of the horizontal advection term. Their conclusion was that this term was not greater than  $30 \text{ W m}^{-2}$  in magnitude. They recorded cold advection at night because of drainage flows and warm advection during the day because of onshore flows during this wintertime period. In the present study of a summertime coastal city, the sea-breeze régime determines the flow during afternoon periods, which contributes to large horizontal advection of heat and moisture. In this work, the consistency between measurements and the numerical simulation of horizontal advection is of major interest since it gives a higher confidence in the estimates. This supports the use of numerical simulation as a tool in future studies to optimize the location of instruments and to interpret observations from a field campaign.

## 6 Conclusion

The present study applies the volumic approach proposed by Lee (1998) to the measurement of heat and moisture fluxes over the dense old core of a coastal European city. A quantification of the contributions of the different processes that take place in the atmospheric layer between the mean building height and the top of a measurement tower is performed with the available measurements and an atmospheric numerical simulation evaluated against observations of Lemonsu et al. (2006). During the period analyzed, a sea-breeze régime developed each day, and it is shown that the contribution of horizontal advection on sensible heat and moisture fluxes is preponderant during the period of the sea-breeze flow. For heat a more complete analysis is conducted, and a specific framework is developed to estimate vertical advection. A first term is associated with the WPL vertical velocity, and a second term results from horizontal wind divergence. This last term is found to be a non-negligible term but does not reach the magnitude of the horizontal advection. Contribution of radiative divergence has been computed using a radiative transfer model and the absorption of upward longwave radiation by the superadiabatic surface layer can reach up to  $30 \text{ W m}^{-2}$  at midday. This term is not significantly modified by urban emissions of carbon dioxide or aerosol particles.

Comparisons are presented between the measured and modelled estimates of horizontal advection. The good consistency between these two independent estimations

gives more confidence to the conclusions. It also proves that the numerical simulation is a useful tool to help with site selection in order to find locations where such effects could be avoided or minimized. The model can also be used as in this study to analyze the measurements and highlight the processes that lead to the observed fluxes.

**Acknowledgements** The UBL project has been funded by the CNRS program for atmospheric dynamics PATOM. We acknowledge F. Lohou and A. Coppalle who operated OBS and GLM sites. We also acknowledge the helpful discussions with M.W. Rotach concerning the choice of the best suited wind profile in the roughness sublayer. We thank the referees for helpful comments on the manuscript

## References

- Aubinet M, Berbigier P, Bernhofer C, Cescatti A, Feigenwinter C, Granier A, Grünwald T, Havrankova K, Heinesch B, Longdoz B, Marcolla B, Montagnani L, Sedlak P (2005) Comparing CO<sub>2</sub> storage and advection conditions at night at different Carboeuroflux sites. *Boundary-Layer Meteorol* 116:63–94
- Aubinet M, Heinesch B, Yernaux M (2003) Horizontal and vertical CO<sub>2</sub> advection in a sloping forest. *Boundary-Layer Meteorol* 108:397–417
- Baldocchi D, Finnigan J, Wilson K, Paw U KT, Falge E (2000) On measuring net ecosystem carbon exchange over tall vegetation on complex terrain. *Boundary-Layer Meteorol* 96:257–291
- Businger J (1982) The fluxes of specific enthalpy, sensible heat and latent heat near the earth's surface. *J Atmos Sci* 39:1889–1893
- Coceal O, Belcher S (2004) A canopy model of mean winds through urban areas. *Quart J Roy Meteorol Soc* 130:1349–1372
- Cros B, Durand P, Cachier H, Drobinski P, Fréjafon E, Kottmeier C, Perros PE, Peuch VH, Ponche JL, Robin D, Saïd F, Toupance G, Wortham H (2004) The ESCOMPTE program: an overview. *Atmos Res* 69:241–279
- Feigenwinter C, Bernhofer C, Vogt R (2004) The influence of advection on short term CO<sub>2</sub> budget in and above a forest Canopy. *Boundary-Layer Meteorol* 113:201–224
- Finnigan J (1999) A comment on the paper by Lee (1998): On micrometeorological observations of surface-air exchange over tall vegetation. *Agric For Meteorol* 97:55–64
- Finnigan J (2004) A re-evaluation of long-term flux measurement techniques Part II: coordinate systems. *Boundary-Layer Meteorol* 113:1–41
- Frangi J, Druihet A, Durand P, Ide H, Pages J, Tinga A (1992) Energy budget of the Sahelian surface layer. *Ann Geophys* 10(1/2):25–33
- Grimmond CSB, Salmond JA, Oke TR, Offerle B, Lemonsu A (2004) Flux and turbulence measurements at a densely built-up site in Marseille: heat, mass (water and carbon dioxide), and momentum. *J Geophys Res (D Atmos)* 109(D24101), doi: 10.1029/2004JD004936.
- Ha K, Mahrt L (2003) Radiative and turbulent fluxes in the nocturnal boundary layer. *Tellus* 55A: 317–327
- Kohsiek W, Liebenthal C, Foken T, Vogt R, Oncley SP, Bernhofer Ch, DeBruin HAR (2007) The Energy Balance Experiment EBEX-2000, Part III: Behaviour and quality of the radiation measurements. *Boundary-Layer Meteorol* DOI: 10.1007/s10546-006-9135-8
- Lafore JP, Stein J, Asencio N, Bougeault P, Ducrocq V, Duron J, Fischer C, Hérelil P, Mascart P, Masson V, Pinty JP, Redelsperger JL, Richard E, de Arellano JV-G (1998) The Méso-NH atmospheric simulation system. Part I: adiabatic formulation and control simulation. *Ann Geophys* 16:90–109
- Lee X (1998) On micrometeorological observations of surface-air exchange over tall vegetation. *Agric For Meteorol* 91:39–49
- Lee X, Hu X (2002) Forest-air fluxes of carbon, water and energy over non-flat terrain. *Boundary-Layer Meteorol* 103:277–301
- Lee X, Massman W, Law B (2004) Handbook of micrometeorology: a guide for surface flux measurement and analysis. Springer-Verlag, Heidelberg, 264 pp
- Lemonsu A, Grimmond CSB, Masson V (2004) Modeling the surface energy balance of the core of an old mediterranean city: Marseille. *J Appl Meteorol* 43:312–327
- Lemonsu A, Pigeon G, Masson V, Moppert C (2006) Sea–town interactions over Marseille: 3D urban boundary layer and thermodynamic fields near the surface. *Theor and Appl Climatol* 84(6): 171–178

- Mallet M, Roger J, Despiaud S, Dubovik O, Putaud J (2003) Microphysical and optical properties of aerosol particles in urban zone during ESCOMPTE. *Atmos Res* 69:73–97
- Masson V (2000) A physically-based scheme for the urban energy budget in atmospheric models. *Boundary-Layer Meteorol* 94:357–397
- Masson V, Grimmond CSB, Oke TR (2002) Evaluation of the Town Energy Balance (TEB) scheme with direct measurements from dry districts in two cities. *J Appl Meteorol* 41:1011–1026
- Mestayer PG, Durand P, Augustin P, Bastin S, Bonnefond JM, Bénech B, Campistron B, Coppalle A, Delbarre H, Dousset B, Drobinski P, Druilhet P, Fréjafon E, Grimmond CSB, Groleau D, Irvine M, Kergomard C, Kermadi S, Lagouarde JP, Lemonsu A, Lohou F, Long N, Masson V, Moppert C, Noilhan J, Offerle B, Oke TR, Pigeon G, Puygrenier V, Roberts S, Rosant JM, Saïd F, Salmund J, Talbaut M, Voogt J (2005) The urban boundary-layer field campaign in Marseille (UBL/CLU-Escompte): set-up and first results. *Boundary-Layer Meteorol* 114:315–365
- Mlawer E, Taubman S, Brown P, Iacono M, Clough S (1997) Radiative transfer for inhomogeneous atmospheres: RRTM, a validated correlated-k model for the longwave. *J Geophys Res* 102(D14):16663–16682
- Noilhan J, Mahfouf JF (1996) The ISBA land surface parameterisation scheme. *Global Planet Change* 13:145–159
- Oke TR (1976) The distinction between the canopy and boundary-layer urban heat islands. *Atmosphere* 14:268–277
- Oke TR (1988) The urban energy balance. *Prog Phys Geogr* 12:471–508
- Oke TR (2004) Urban observations. IOM Report No. 81 WMO/TD No. 1250, World Meteorological Organization, Geneva. 49 pp
- Paw U KT, Baldocchi DD, Meyers TP, Wilson KB (2000) Correction of eddy-covariance measurements incorporating both advective effects and density fluxes. *Boundary-Layer Meteorol* 97:487–511
- Pigeon G, Lemonsu A, Long N, Barri J, Durand P, Masson V (2006) Urban thermodynamic island in a coastal city analyzed from an optimized surface network. *Boundary-Layer Meteorol* 120:315–351
- Raupach MR, Legg BJ, Edwards I (1980) A wind tunnel study of turbulent flow close to regularly arrayed rough surface. *Boundary-Layer Meteorol* 18:373–397
- Roger J, Mallet M, Dubuisson P, Cachier H, Vermote E, Dubovik O, Despiaud S (2006) A synergetic approach for estimating the local direct aerosol forcing: application to an urban zone during the Expérience sur Site pour Contraindre les Modèles de Pollution et de Transport d'Emission (ESCOMPTE) experiment. *J Geophys Res* 111(D13208):13208–13216
- Rotach MW (1993) Turbulence close to a rough urban surface. Part I: Reynolds stress. *Boundary-Layer Meteorol* 65:1–28
- Rotach MW (2001) Simulation of urban-scale dispersion using a lagrangian stochastic dispersion model. *Boundary-Layer Meteorol* 99:379–410
- Rotach MW, Calanca P, Weigel A, Andretta M (2003) On the closure of the surface energy balance in highly complex terrain. In: ICAM/MAP. Brig (CH), pp 247–250
- Roth M (2000) Review of atmospheric turbulence over cities. *Quart J Roy Meteorol Soc* 126:941–990
- Savijärvi H (2006) Radiative and turbulent heating rates in the clear-air boundary layer. *Quart J Roy Meteorol Soc* 132:147–161
- Spronken-Smith RA, Kossmann M, Zawar-Reza P (2006) Where does all the energy go? Surface energy partitioning in suburban Christchurch under stable wintertime conditions. *Theor Appl Climatol* 84(1–3):137–149
- Stull R (1988) An introduction to boundary layer meteorology. Kluwer Academic Publishers, Dordrecht, 666 pp
- Voogt JA, Grimmond CSB (2000) Modeling surface sensible heat flux using surface radiative temperatures in a simple urban area. *J Appl Meteorol* 39:1679–1699
- Webb EK, Pearman GI, Leuning R (1980) Correction of flux measurements for density effect due to heat and water vapour transfer. *Quart J Roy Meteorol Soc* 106:85–100